Partitioning of ribonucleoprotein complexes from the cellular actin cortex

C. Isaac Angert[1], Siddarth Reddy Karuka[1], Louis M. Mansky[2,3,4], Joachim D. Mueller[1,2,5]
School of Physics and Astronomy[1], University of Minnesota, Minneapolis, MN 55455
Institute of Molecular Virology[2], University of Minnesota, Minneapolis, MN 55455
Division of Basic Sciences, School of Dentistry[3], University of Minnesota, Minneapolis, MN 55455
Masonic Cancer Center[4], University of Minnesota, Minneapolis, MN 55455
Department of Biomedical Engineering[5], University of Minnesota, Minneapolis, MN 55455

Abstract

The cell cortex plays a crucial role in cell mechanics, signaling, and development. However, little is known about the influence of the cortical meshwork on the spatial distribution of cytoplasmic biomolecules. Here, we describe a new fluorescence microscopy method to infer the intracellular distribution of labeled biomolecules with sub-resolution accuracy. Unexpectedly, we find that RNA-binding proteins are partially excluded from the cytoplasmic volume adjacent to the plasma membrane that corresponds to the actin cortex. Complementary diffusion measurements of RNA-protein complexes suggest that a rudimentary model based on excluded volume interactions can explain this partitioning effect. Our results suggest the actin cortex meshwork may play a role in regulating the biomolecular content of the volume immediately adjacent to the plasma membrane.

Teaser

A novel microscopy technique reveals partial exclusion of RNA-protein complexes from the actin cortex due to their large hydrodynamic size.

Introduction

Both the actin cortex and RNA are fundamental building blocks of eukaryotic cells. The cortex, acting in concert with other cytoskeletal elements, is involved in nearly all aspects of cell mechanics, such as cell structure, membrane rigidity, migration and division (1). Due to its location adjacent to the plasma membrane, the cortex plays important roles in signal transduction and mechanical response pathways (1, 2). In contrast, RNA molecules serve as genomic messengers and constitute major components of the cellular translational machinery. Specific localization of mRNA to sub-cellular regions has been widely observed (3). RNA localization to sub-cellular compartments such as the endoplasmic reticulum (ER),

processing (P)-bodies or distal cytoplasm in neurons is critical to aspects of development (4) and is an important regulator of cellular function (5). Due to their highly structured and extended nature, mRNAs have hydrodynamic radii that are dramatically larger than those of the globular proteins they encode (6). Based on a recent study (7), a typical mRNA of 1 – 2 kilobase length (8, 9) is expected to have a hydrodynamic radius in the range of ~10 nm. The radii of ribosomes are of comparable size (10 – 15 nm) (10, 11).

Previous biophysical studies have established that the cell cytoplasm is a complex medium (12, 13) that modulates the diffusion and localization of large (>10 nm) particles in a size-dependent manner (14–18). These observations have prompted the question of whether the large size of the cellular translational machinery might broadly influence its subcellular localization (19). Here, the novel observation that large riboneucleoprotein (RNP) complexes are partially excluded, or partitioned, from the interior of the actin cortex is reported. These observations are facilitated by recent developments in two-photon dual-color (DC) z-scan fluorescence microscopy (20), which is adapted in the present work to infer protein localizations inside living cells with sub-diffraction resolution. DC z-scans are acquired by moving the two-photon excitation volume vertically through the cytoplasm of adherent cells. This movement of the excitation volume yields fluorescent intensity traces that encode the vertical intracellular distribution of a fluorescently labeled protein species as well as that of a distinctly colored reference fluorescent protein. Although different reference species are possible, our typical choice is a soluble, purely cytoplasmic protein, which serves as a “paint” that marks the cytoplasmic extent. Differential vertical localization between the fluorescently labeled protein and the reference protein is encoded as subtle differences in the shape of the DC z-scan traces. The magnitude of the differential vertical localization is quantitatively recovered from the data by fitting the z-scan traces (20).

Results

Initial proof-of-principle experiments were conducted with U2OS cells to demonstrate the utility of DC z-scan to quantify differences in intracellular protein distributions. For detailed descriptions of the z-scan model geometries used in the following, see the Materials and Methods section. First, cells were co-transfected with mCherry-RXR (a protein that localizes in the nucleus) and EGFP (which diffuses freely throughout the cell). DC z-scans through the cell nucleus were fit to the S^G-S^{CH} (Eq. 17) model to identify the slab length associated with the mCherry fluorescence, which corresponds to the nuclear thickness, and the slab length of the EGFP signal, which corresponds to the slightly longer thickness of the entire cell (Fig. 1A). A representative z-scan with fit shows that the mCherry-RXR and EGFP z-scans are well described by this

model, with flat residuals and $\chi_v^2 = 1.2$ (Fig. 1B). The fit identified the intensity amplitudes of mCherry-RXR and EGFP, the locations of the bottom and top cell edges (a^G = 2.16 µm and b^G = 5.80 µm), as well as the locations of the bottom and top nuclear edges (a^{CH} = 2.51 µm and b^{CH} = 5.03 µm), respectively. The distances between the edges of the EGFP and mCherry slab were defined at the top and bottom of the cell by $\Delta^T = b^{CH} - b^G$ = -770 nm and $\Delta^B = a^G - a^{CH}$ = -350 nm, respectively. Since Δ measures the displacement between the borders of the EGFP and mCherry layers, its value can be positive or negative in general. Distances are reported by taking the absolute value $|\Delta|$, which in this instance determines the thickness of the cytoplasmic layers surrounding the top and bottom of the nucleus (Fig. 1A). Repeated DC z-scan experiments on multiple cells yielded multiple estimates of Δ^T and Δ^B which are summarized by a histogram (Fig. 1C) with averages of $\langle\Delta^T\rangle$ = -340 ± 50 nm and $\langle\Delta^B\rangle$ = -260 ± 30 nm (SEM, n = 19).

As a control, DC z-scans were performed through the cytoplasm of U2OS cells co-expressing EGFP and mCherry fluorescent proteins (Fig. 1D). Since both proteins are soluble species within the cell cytoplasm, DC z-scans are expected to recover Δ = 0, on average. As shown in Fig. 1E, a representative DC z-scan fits to a S^G-S^{CH} (Eq. 17) model with flat residuals and $\chi_v^2 = 1.1$. Repeated DC z-scans in multiple cells recovered $\langle\Delta^B\rangle$ = -2.3 ± 1.2 nm and $\langle\Delta^T\rangle$ = 1.0 ± 3.1 nm (SEM, n = 59). The histogram of the combined displacements is shown in Fig. 1F. For the EGFP and mCherry co-expression, the weighted average of the combined data yielded $\langle\Delta\rangle$ = -0.5 ± 1.7 nm (SEM, n = 118), which is consistent with Δ = 0 nm within 0.3 SD. Note that since the diameter of globular proteins is typically several nanometer, differences of less than 10 nm were considered insignificant in this study and treated as consistent with zero.

Next, DC z-scans were performed in U2OS cells co-expressing EGFP-HRas and mCherry (Fig. 1G). EGFP-HRas was previously reported to be a peripheral membrane protein that binds to the plasma membrane as a monomer (*21*). Previous z-scan studies established that the axial distribution of EGFP-HRas in the cytoplasm and at the PM membranes was successfully modeled by the δSδ layer geometry (*21*, *22*). Thus, DC z-scans from cells co-expressing mCherry and EGFP-HRas were modeled by the $(S^{CH}\text{-}\delta S\delta)^G$ geometry (Eq. 17). A fit of a representative z-scan attained good quality of fit with $\chi_v^2 = 1.2$ and flat residuals. Repeated z-scans in the cytoplasm of multiple cells co-expressing EGFP-HRas and mCherry (Fig. 1I) determined $\langle\Delta\rangle$ = -2.6 ± 5.4 nm (SEM, n = 30), which was within 0.5 SD of the expected value of Δ = 0. This result indicated that the location of the cytoplasm slab edge, as determined by fitting the soluble mCherry species to the S model, coincided with the location of the PM, as determined by fitting the EGFP-HRas species to the δSδ model.

Next, the axial cytoplasmic distribution of APOBEC 3G (A3G) labeled with EGFP and co-expressed with mCherry (Fig. 1J) was examined. A representative z-scan acquired in the cytoplasm of a HeLa cell showed a single broad peak for both mCherry and A3G-EGFP (Fig. 1K). Since the trace shape was suggestive of a slab geometry, both species were fit to slab models (S^{CH}-S^{G}, Eq. 17). This fit provided a good description of the DC z-scan intensity profiles with χ_v^2 = 1.3 and flat residuals (Fig. 1K). Interestingly, this fit identified non-zero values for the displacements at the top and bottom PM (Δ^B = 184 nm and Δ^T = 167 nm). Repeated z-scan acquisitions at the same location in this cell determined $\overline{\Delta^B}$ = 180 ± 6 nm and $\overline{\Delta^T}$ = 162 ± 12 nm (SEM, n = 12). This surprising observation suggests that the thickness of the soluble A3G-EGFP layer is less than the thickness of the mCherry layer, unlike the results obtained for EGFP and mCherry (Fig. 1D), which had equal lengths (Δ = 0) for both soluble proteins. Repeated z-scan acquisitions in multiple HeLa cells (Fig. 1L) found $\langle\Delta\rangle_{HeLa}$ = 155 ± 10 nm (SEM, n = 64), indicating that A3G does not occupy the entire cytoplasmic volume. To further validate this observation, DC z-scan measurements were collected using a different cell line (U2OS), which resulted in $\langle\Delta\rangle_{U2OS}$ = 110 ± 9 nm (SEM, n = 32).

Intriguingly, this result implies that cytoplasmic A3G-EGFP was excluded from regions adjacent to the PM with apparent thickness of 100 - 200 nm. Given the magnitude of this value and its differential value in U2OS and HeLa cell lines, further experiments were conducted to test whether A3G-EGFP might be partially excluded from the dense meshwork of the actin cortex. To do this, HeLa cells were treated with ethanol (see Materials and Methods), which disrupts actin assemblies and leads to the formation of large plasma membrane blebs (*23*) (Fig. 2A) that lack an intact actin cortex (*24–26*). A representative z-scan performed near the center of these blebs showed good quality of fit to a S^{CH}-S^{G} model (Eq. 17 and Fig. 2C). Repeated z-scans in blebs from HeLa cells co-expressing A3G-EGFP and mCherry determined $\langle\Delta\rangle$ = 31 ± 10 nm (SEM, n = 14), which differs from the results obtained in untreated HeLa cells by 8.8 SD. The distribution of Δ in blebs and in untreated cells are markedly different (Fig. 2D). The strong reduction in Δ found in blebs supports the conclusion that A3G-EGFP concentration is depleted from the vicinity of the PM by the presence of the actin cortex. To reflect these results Δ is also referred to as the effective depletion length.

Given that dependence of cortical architecture on the cell type has been observed (*27–29*), the differences in effective depletion length observed between HeLa and U2OS cells might reflect natural differences in cortex thickness between these cell types. To investigate this, direct measurements of the cortex thickness were performed using distinct fluorescent colors to mark the actin cortex and the plasma

membrane. A previous study used this approach to estimate the actin cortex thickness from the displacement between intensity peaks corresponding to the actin and the PM marker in confocal images (*30*). In the present study two-photon DC z-scan was employed instead of confocal imaging to determine the cortex thickness from the intensity profiles of EGFP-HRas (which binds to the PM) and Lifeact-mApple (which binds to actin and marks the cortex) (*31*) by fitting to on a quantitative model of the entire intensity traces (Fig. 3A). The axial concentration profile of both labels is depicted in Fig. 3B, which shows an enrichment of EGFP-HRas and Lifeact-mApple at the PM and within the cortex, respectively. A small amount of both fluorescent proteins is also present in the cytoplasm. Based on this profile, EGFP-HRas is again modeled by the δSδ geometry. The distance separating the two HRas δ layers represents the cell thickness L_{cell}.

The concentration profile of Lifeact-mApple implies a wide cytoplasmic slab of length L_{cyto} separating two thin slabs representing the cortex at the bottom and the top membrane with thickness L_C^B and L_C^T (Fig. 3B), giving rise to an SSS^{CH} (triple S-layer) geometry. Choosing a uniform slab with a sharp transition between the cortical and cytoplasmic spaces to model the cortex has been previously used in (*30*) where it is estimated that even a substantial non-uniformity of the cortical density leads to only a small change in the estimated cortex thickness. Because the expected slab length L_C of the cortex is smaller than 500 nm, its length cannot be directly identified in single-color (SC) z-scan experiments. Such thin slabs are experimentally indistinguishable from a δ layer (*32*). However, the centroid position of the thin cortical layer is expected to coincide with the midpoint of the slab as depicted in Fig. 3B. Given this, modeling the Lifeact-mApple species as a $\delta\text{S}\delta^{\text{CH}}$ geometry can identify the cortex centroid from the fitted location of each δ layer. Combined with the EGFP-HRas species, this DC z-scan fit ($\delta\text{S}\delta^{\text{CH}}$-$\delta\text{S}\delta^{\text{G}}$) identifies the locations of the δ layers corresponding to the cortex centroid and the PM as well as their displacement Δ. The distance $|\Delta|$ separating both δ layers is half of the actin cortex thickness, $|\Delta| = L_C / 2$ (Fig. 3B).

The relation $|\Delta| = L_C / 2$ was verified by computer modeling of the DC z-scan intensity profile of the SSS^{CH}-$\delta\text{S}\delta^{\text{G}}$ geometry (Fig. 3B), while systematically varying the cortical thickness $L_{C,in}$, as well as the cell thickness and fluorescence intensities of HRas and Lifeact (see Materials and Methods). These simulated scans were fit to a $\delta\text{S}\delta^{\text{CH}}$- $\delta\text{S}\delta^{\text{G}}$ model to determine the locations of each δ layer. The difference Δ between the fitted cortical δ layer and the PM δ layer was computed for each fit and the averaged Δ recovered from fits to simulated DC z-scans were plotted as a function of the cortical thickness $L_{C,in}$ (Fig. S1). The data

confirm that the relation $|\Delta| = L_C / 2$ is accurate to within 10 nm for cortex thicknesses up to 200 nm. This result demonstrates that this approach is experimentally accurate and produces negligible error.

Repeated DC z-scans were then collected in cells co-expressing EGFP-HRas and Lifeact-mApple proteins in order to determine cortical thickness. A representative DC z-scan and fit to the $\delta S\delta^{CH}$- $\delta S\delta^{G}$ model (Fig. 3C) for both proteins is shown in Fig. 3D. Data taken from multiple cells resulted in absolute values $|\langle\Delta\rangle|_{U2OS}$ = 63 ± 8 nm (SEM, n = 7) and $|\langle\Delta\rangle|_{HeLa}$ = 100 ± 13 nm (SEM, n = 15). These values correspond to uniform cortex thicknesses of 126 ± 16 nm for U2OS cells and 200 ± 24 nm for HeLa cells (Fig. 3E).

Since both the depletion length Δ for A3G-EGFP and the cortex thickness differed between the two cell lines, $\langle\Delta\rangle$ in HeLa and U2OS cells were plotted for comparison (Fig. 3F). DC z-scans were performed in HeLa and U2OS cells expressing additional proteins, HIV-1 Gag^{G2A}-EGFP, and its matrix (MA) domain, MA^{G2A}-EGFP (*33*) with mCherry again as a reference marker of the cytoplasmic volume for each instance. A cell-line dependent $\langle\Delta\rangle$ was observed for both proteins (Fig. S2), and their $\langle\Delta\rangle$ values were added to Fig. 3F. Interestingly, all 3 data points cluster near a line of slope 0.66, indicating that, although the magnitude of the depletion effect varies for each protein, it is systematically scaled by ~66% between these two cell lines. This same ratio corresponds well to the cortex thickness ratio estimated by DC z-scan between HeLa and U2OS cells (0.66 ± 0.11, shaded area in Fig. 3F), suggesting that the cell-type dependent differences in $\langle\Delta\rangle$ are due to differences in their cortical actin thicknesses. This result further implicates the actin cortex as a central driver of the observed depletion effect near the PM.

All 3 proteins in Fig. 3F are known to be RNA-interacting proteins: HIV-1 Gag^{G2A} binds specifically and non-specifically to RNA sequences through basic residues and two zinc fingers in its nucleocapsid (NC) domain (*34–36*), while the MA domain of Gag separately interacts with RNA via a stretch of basic residues in its highly basic region (HBR) (*37–39*) and has preferential tRNA binding affinity (*40*, *41*). A3G interacts with RNA primarily through its N-terminal domain zinc finger (*42*, *43*). A3G-RNA binding is required for packaging of A3G into retroviral particles (*43–46*) and is critical to its antiretroviral activity (*43*, *44*). To test whether the depletion effect is specific to RNA-binding proteins, measurements with two EGFP-labeled proteins that lack a known RNA binding function were conducted. In particular, DC z-scans of HeLa cells co-expressing mCherry with the GABA-A receptor associated protein fused to EGFP (GABARAP-EGFP), and mCherry with a tandem hexamer of the Venus fluorescent protein, $Venus_6$ were collected. The average $\langle\Delta\rangle$ value of both proteins was found to be < 10 nm (Fig. 4A) and therefore treated as consistent with zero. The

previously presented depletion lengths in HeLa cells from Fig. 3D were added to Fig. 4A to highlight the contrast with the RNA-binding proteins. Since RNA binding appeared to be important for observing depletion, DC z-scans were performed with the mutant A3G^{C97A}-EGFP, which has impaired RNA binding due to mutation of the N-terminal zinc finger (*44*). These measurements revealed a large reduction in <*Δ*> compared to that of wildtype A3G-EGFP (Fig. 4A). Lastly, the <*Δ*> value was measured in mCherry expressing HeLa cells that were stained with the small molecule RNA binding dye, SYTO RNASelect. These measurements revealed that the labeled cellular RNA had a significant degree of depletion adjacent to the PM (Fig. 4A).

Based on these results, it was hypothesized that the exclusion of large RNA species from the dense cortical meshwork may be responsible for the observed PM adjacent depletion of RNA binding proteins (Fig. 4B). The average pore diameter of the actin cortex has been reported to range between 50 to 200 nm (*28*), depending on cell type. These values are only slightly larger than or overlap with the size of large RNAs (*6*, *7*). Thus, a partial partitioning of RNAs from the interior of the cortex could be driven by excluded volume interactions. In a simple model of the cortical partitioning (Fig. 4C), the ratio of the concentration c_C in the cortical layer to the concentration c_{cyto} in the cytoplasm defines the partition coefficient $R_C = c_C / c_{\text{cyto}}$. This partitioning of the protein concentration between the cytoplasmic and cortical spaces introduces a SSS^G concentration profile for the EGFP-labeled RNA-binding protein (Fig. 4C), which consists of two thin cortical slabs of length L_C^B and L_C^T separated by a thick cytoplasmic slab of length L_{cyto} with a higher protein concentration. As in the case of the Lifeact measurements (Fig. 3), the cortical layer is too narrow to be directly resolved by z-scan analysis. However, since the concentration within the cortex layer is reduced (Fig. 4C), the z-scan intensity profile can be effectively approximated by a single slab layer with a width that slightly exceeds the cytoplasmic thickness L_{cyto} (Fig. 4D). Consequently, the apparent depletion lengths Δ^B and Δ^T will be less than the corresponding cortex thickness L_C^B and L_C^T in a manner that depends on R_C.

To quantitatively analyze how *Δ* recovered from DC z-scans is related to R_C and L_C, simulation of DC z-scan traces for an SSS^G-S^{CH} geometry was performed (see Materials and Methods). These simulated traces were fit to the S^{CH}-S^G DC z-scan model (Fig. 4D). The cortex length L_C and partition ratio R_C (Fig. 4C) were varied for each simulation and the averaged *Δ* recovered from the fits was plotted (Fig. 4E, diamonds). The results of these simulations indicate a nearly linear relationship between *Δ* and R_C for a given L_C. This linear relationship can also be derived from preserving the integrated area Λ under the z-scan intensity

profile between the SSS^G model and the fitted S^G model. Since Λ and the axially integrated concentration A are directly proportional (Eq. 11), the concentration areas of both models (Fig. 4C and D) must match. In particular, the cortical concentration area $A_C^i = L_C^i \cdot c_C$ (Fig. 4C) has to be equal to the added extra area $A_x^i = L_C^i \cdot R_C c_{cyto}$ (Fig. 4D) at both the top (i = T) and bottom (i = B) of the cell, which predicts an apparent depletion length *Δ* (Fig. 4D) of

$$\Delta = \left(1 - R_C\right) L_C \,, \qquad 1$$

where the superscript has been omitted. This model (Fig. 4E, solid lines) is in excellent agreement with the results from the simulations. Eq. 1 was used to estimate the partition coefficient of proteins from their measured depletion lengths (Fig. 3D) using the experimentally determined cortex thicknesses L_C. R_C = 0.76 ± 0.02, 0.35 ± 0.04, and 0.24 ± 0.05 for MA^{G2A}-EGFP, Gag^{G2A}-EGFP, and A3G-EGFP, respectively were determined from HeLa cells. Similar values (0.76 ± 0.02, 0.41 ± 0.02, and 0.17 ± 0.07) were obtained from the measurements in U2OS cells.

Because these estimates of the partition coefficient R_C rely on the measured displacement *Δ*, which is a new method, a second approach was developed to estimate R_C independently of *Δ* by using DC z-scans in very thin cytoplasmic regions. The partial exclusion of fluorescently labeled protein from the cortex reduces the fluorescence area Λ^G as compared to the area Λ_{ref}^G corresponding to the hypothetical case of no exclusion. The ratio of these two areas is denoted as the axially averaged partition coefficient,

$$\bar{R}_z = \frac{\Lambda^G}{\Lambda_{\mathrm{ref}}^G} = \frac{A^G}{A_{\mathrm{ref}}^G} = \frac{L_{cyto} c_{cyto} + 2 L_C R_C c_{cyto}}{L_{cell} c_{cyto}} \,, \qquad 2$$

where the proportionality between Λ and A (Eq. 11) was used to express the ratio in terms of the integrated concentration areas. Since the cell thickness is defined by (Fig. 3B),

$$L_{cell} = L_{cyto} + L_C^T + L_C^B = L_{cyto} + 2 L_C \,, \qquad 3$$

where $L_C = (L_C^T + L_C^B)/2$ defines the average cortex thickness, the axially averaged partition coefficient simplifies to

$$\bar{R}_z = 1 + (R_C - 1) \frac{2 L_C}{L_{cell}} \qquad 4$$

This equation predicts $\bar{R}_z \to 1$ for very thick sections ($L_{cyto} \gg L_C$). As the cell thickness L_{cell} decreases, the value of $\bar{R}_z$ drops. It reaches a limiting value of $\bar{R}_z = R_C$ for very thin cell section composed entirely of cortex $L_{cell} = 2L_C$. Thus, DC z-scans in thin regions near the cell perimeter combined with DC z-scans in thick regions of the same cells allow direct estimation of the partition coefficient.

While this relatively simple model sets a minimum cell thickness of $L_{cell} = 2L_C$, where L_C denotes the average cortical thickness in a given cell type, very thin cellular regions were found where the realized cell thickness is less than this value, $L_{cell} < 2L_C$. This implies that in these regions of the cell the local cortex thickness is less than L_C. Assuming that these thin sections are composed entirely of cortex, Eq. 4 is generalized to,

$$\bar{R}_z = \begin{cases} R_C & \text{if} \quad L_{cell} < 2L_C \\ 1 + (R_C - 1)\dfrac{2L_C}{L_{cell}} & \text{if} \quad L_{cell} > 2L_C \end{cases} . \qquad 5$$

As shown in Fig. 5A & B, cytoplasmic DC z-scans in thick and thin regions of a cell co-expressing EGFP and mCherry indicate that the relative concentrations of the EGFP and mCherry species are identical regardless of cytoplasm thickness. In contrast, cytoplasmic DC z-scans in thick and thin regions of a cell co-expressing HIV-1 Gag^{G2A}-EGFP and mCherry show that the relative intensity of Gag^{G2A}-EGFP is sharply reduced in thin regions (Fig. 5C & D), demonstrating that the depletion effect is reflected in the decrease of the integrated fluorescence area Λ^G as a function of thickness. To quantify the effect and utilize Eq. 2, an estimate was needed for the reference area $\Lambda^G_{ref} = L_{cell} g^G_{cyto}$, where $g^G_{cyto} = c^G_{cyto}\eta$ (Eqs. 11 and 2). The cell thickness L_{cell} was determined from the mCherry signal in the red detection channel as described in the Material and Methods, while the amplitude g^G_{cyto} was estimated from a scan through a thick cell section (L_{cell} > 1.5 µm) where g^G_{cyto} can be reliably extracted from fitting the DC z-scan traces. Repeated z-scans were performed within the same cell covering thick and thin regions (Fig. 5E) to graph $\bar{R}_z = \Lambda^G / \Lambda^G_{\text{ref}}$ versus L_{cell}. As expected, $\bar{R}_z$ is approximately one for a HeLa cell coexpressing mCherry and EGFP (Fig. 5F), which implies the absence of partitioning of EGFP from the cortex according to Eq. 5 ($R_C = 1$). In contrast, DC z-

scan estimates of $\bar{R}_z$ for Gag^{G2A}-EGFP for a HeLa cell (magenta diamonds) and a U2OS cell (blue diamonds) exhibit a decrease at thin cell sections (Fig. 5F). The HeLa cell data in Fig. 5F closely resemble the simple model (Eq. 5), and cluster near 0.2 for $L_{cell} < L_C$, suggesting a cortical partition coefficient near 0.2 in this cell line. The data from U2OS cells appears to deviate from (Eq. 5) in thin cell sections, which may reflect the presence of distinct peripheral F-actin structures in this cell line as discussed later.

The cortical partitioning effect documented here supports a model where protein depletion within the cortex is driven by protein association into ribonucleoprotein complexes that are much larger than the typical protein. In such a case, the large <*Δ*> values should be correlated with substantially slowed cytoplasmic diffusion. FCS measurements were performed in HeLa cells in order to estimate the effective diffusion coefficient D_{eff} of labeled proteins in the cytoplasm (see Materials and Methods). In Fig. 6A <*Δ*> values from Fig. 4 were plotted versus the median D_{eff} that was obtained from FCS measurements. Two other members of the APOBEC3 protein family, A3A-EGFP and A3C-EGFP, which have differing antiretroviral activities (*47–49*), were also measured and added to Fig. 6A. These data show that large <*Δ*> values are associated with remarkably low cytoplasmic mobility. This relationship is summarized by the cartoons in Fig. 6 B&C. In order to model the data in Fig. 6A, the cortical partitioning was described as arising from excluded volume interactions of particles that are allowed to enter spherical voids (*50–52*),

$$R_C = (1 - r_p / r_v)^3 \,, \qquad 6$$

where r_p is the particle radius, and r_v is the void radius. A hindered cytoplasmic diffusion coefficient D_{eff} was modeled as arising from a size-dependent viscosity imposed by macromolecular crowding within the cytoplasm (*53*, *54*) according to

$$\frac{D_{eff}}{D_0} = \exp\left[-\left(\frac{r_{eff}}{\xi} \right)^a \right], \qquad 7$$

where D_0 is a reference diffusion coefficient, r_{eff} is an effective hydrodynamic radius of the diffusing particles, a is a scaling exponent of order 1, and ξ is a length interpreted as the characteristic distance between points of entanglement within the crowded solution. Along with equation 1, setting $r_{eff} = r_p$ in the above yields a relation between D_{eff} and Δ,

$$\Delta = L_c\left[1-\left(1-\xi/r_v \ln\left(D_0/D_{eff}\right)^{1/a}\right)^3\right]. \qquad 8$$

This curve is plotted as the magenta line in Fig. 6A using values L_C = 170 nm, D_0 equal to D_{eff} measured for EGFP (27.5 $\mu m^2 s^{-1}$), r_v = 60 nm, ξ = 4 nm and a = 0.7. The values for ξ and a are within the range estimated by (*53*) for HeLa cells. r_v is similar to published estimates of the cortical mesh size (*28*).

Cytoplasmic crowding in cell associated PM blebs may differ from crowding within undisturbed cytoplasm due at least in part to the lack of a cytoskeletal mesh in the bleb interior. Thus, the mobility of A3G-EGFP in HeLa cell blebs was investigated. FCS measurements (Fig. 6A, open circle) showed an order of magnitude increase in D_{eff} compared to A3G in the cytoplasm of untreated HeLa cells. This result supports our choice to model cytoplasmic diffusion of RNP complexes as arising from a size-dependent viscosity (Eq. 717). The value from blebs is plotted as an open circle in order to emphasize that the model parameters (especially r_v and ξ) that describe the rest of the data most likely do not describe data from blebs.

It was recently reported that the cytoplasmic diffusion coefficient of fluorescent proteins depended on their net charge, with positively charged proteins diffusing slowly. It was suggested that this slow diffusion was due to transient interactions with large, negatively charged cell components such as RNA and the cytoskeleton (*55*). An examination was performed to determine whether the D_{eff} values in Fig. 6A might be explained by the net charge of each protein-FP fusion. As shown in Fig. S3, the mobility of the proteins in Fig. 6A was only weakly correlated with net charge. Thus, the mobility of these proteins in living cells is likely to be better understood as arising predominantly from their RNA binding function.

Discussion

In this study, DC z-scan microscopy measurements of the fluorescence intensity profiles of green and red labeled proteins provided the foundation for identifying the cortical partitioning effect and allowed its quantitative description through the effective depletion length Δ. Implementation of the DC z-scan measurements using two-photon microscopy eliminates systematic biases, such as chromatic aberration, from the collected data. DC z-scan permitted precise quantification of the relative localizations of fluorescently labeled proteins. These measurements indicated an apparent restriction in the cytoplasmic volume of RNA binding proteins (e.g., A3G and Gag^{G2A}). The partitioning effect was markedly reduced in

ethanol induced cell blebs, which largely lack a cortex (*24–26*) and was observed to be cell-type dependent in a manner that correlated with DC z-scan estimates of cortex thickness in adherent interphase HeLa and U2OS cells. The depletion effect is interpreted as being a partitioning, or partial exclusion, of these proteins from the volume of the actin cortex. Furthermore, Δ values measured for proteins with and without RNA-binding function suggest that the cortical partitioning is driven by association into RNP complexes and is not strongly associated with protein molecular mass or net charge. This conclusion is supported by measurements of the diffusion coefficient, which shows that a marked decrease in mobility is associated with proteins that have the largest values of Δ.

In vitro and in vivo (*56*) observations of actin assemblies suggest that gel-like properties are nearly ubiquitous, including for the actin cortex specifically (*57*). The cortical partitioning effect may be analogous to solute partitioning from the interior of gels, a well-known chemical phenomenon (*58*, *59*). Furthermore, the subcellular heterogeneity driven by the dense cortical environment is reminiscent of those molecular crowding effects which have been reported to drive association or phase separations in cells (*60*, *61*). This suggests that the crowded environment within gels may drive biophysical phenomena similar to, but distinct from those associated with molecular crowding in the cytoplasm. The observation of cortical partitioning described in this report builds on earlier work that found strong exclusion of labeled colloidal particles with radii exceeding ~10 nm from distal regions of mammalian cell cytoplasm, and regions near the centrosome (*15*, *62*). Subsequent studies documented that the distal excluding regions were associated with a dense cytoskeletal mesh and were thinner than non-excluding regions (*62*). These and other observations (*50*) have suggested that this partitioning was driven by the cytoskeletal meshwork.

The cortical partitioning of RNPs described in the present study also leads to strong exclusion from distal regions of the cytoplasm (Fig. 5). However, unlike previous studies, which linked partitioning to the actin cytoskeleton in general, our observations identified the actin cortex as the causative agent of partitioning. Differentiation between the cortical space and the bulk cytoplasm was not previously achieved and probably reflects experimental limitations in these earlier studies, which are overcome by the use of DC z-scan method employed here. Thus, the cortical partitioning of RNPs and the distal exclusion of microinjected particles documented previously (*15*, *63*) likely are manifestations of the same physical phenomenon, namely the size-dependent partitioning of particles from the actin cortex.

The measurement of the actin cortex thickness, L_C, in HeLa (~200 nm) and U2OS (~130 nm) cells in our study represents a novel application of the DC z-scan technique. This application was inspired by a conceptually similar approach based on confocal microscopy that was used to estimate a cortex thickness

of ~190 nm in mitotic HeLa cells (*30*) and of 300 – 400 nm in interphase HeLa cells with imposed spherical shapes (*29*). Interestingly, DC z-scan identified a cortical thickness ≤200 nm for adherent interphase HeLa and U2OS. This is consistent with literature reports which indicate that cortical architecture is strongly associated with cell morphology (*27*, *29*). In particular, cell adhesion and cell spreading on the glass coverslip can result in a thinning of the actin cortex (*27*, *64*).

DC z-scan measurement of the axially averaged partition coefficient $\bar{R}_z$ (Fig. 5E) provided further evidence that partitioning is associated with the cellular cortex as evidenced by the decreasing $\bar{R}_z$ values in increasingly thinner cell sections. The value of $\bar{R}_z$ in very thin cell sections provides a direct estimate of the cortical partition coefficient R_C, assuming that these thin sections are composed entirely of the actin cortical mesh. This R_C value can in turn provide an additional estimate of cortex thickness that does not rely on DC z-scans of cortical Lifeact. Utilizing Eq. 1, the R_C ~0.2 measured for HIV-1 Gag^{G2A}-EGFP in thin sections of HeLa cells would suggest L_C ~170 nm given $\langle\Delta\rangle$ = 135 ± 8 nm observed for HIV-1 Gag^{G2A}-EGFP in thick cytoplasmic DC z-scans in this same cell line. This value of L_C is within 1.3 SD of the value estimated from DC z-scans of Lifeact. The agreement between these two different DC z-scan approaches provides further validation of the DC z-scan technique and demonstrates its utility for interrogating biophysical properties of the bulk actin cortex.

Interestingly, DC z-scan estimates of $\bar{R}_z$ in U2OS cells exhibited more scatter than observed in HeLa cells, particularly in thin cell sections. This may reflect cell-type differences in F-actin assemblies, in particular large structures such as lamellar actin sheets which may be present near the cell periphery. In electron micrographs of F-actin, these lamellae appear distinct from cortical actin fibers (*27*, *65*). Their extensive presence may invalidate the use of Eq. 5 near the periphery of U2OS cells. Future work is needed to investigate whether distinct types of actin structures modulate the cortical partitioning and whether this effect is cell-type and -function dependent.

The strong correlation between the ability of a protein to bind RNA and measured values of $\langle\Delta\rangle$ (Fig. 4A) suggests that many RNA-protein complexes are too large to efficiently enter the dense actin cortical meshwork. The cortical partitioning of RNA-binding proteins measured by DC z-scan is thus interpreted as arising from an underlying partitioning associated with the large RNA species with which these proteins associate. In this framework, DC z-scans of RNA interacting proteins indirectly probe the spatial distribution of cellular RNAs. More directly, when cellular RNA was labeled with an RNA-binding fluorescent dye, DC z-

scan measurements of <*Δ*> revealed that the RNA itself is partitioned from the cortex with R_C in the range 0.35 – 0.2 (given L_C 170 – 200 nm). This R_C value is interpreted as representing the average R_C of a broad spectrum of differently sized cellular RNAs (i.e., mRNAs, tRNAs, etc) and RNP complexes (e.g., ribosomes) with different degrees of cortical penetration. Similarly, the <*Δ*> values for fluorescently labeled proteins likely represent the average R_C of a heterogenous mix of differently sized RNA complexes to which each protein preferentially binds. Alternatively, it is possible that different <*Δ*> values represent differing levels of RNA-bound and -unbound protein, where the unbound state is identified as the non-partitioned fraction. However, the unbound protein population is expected to be negligible in many cases. This follows from the high concentration of protein-RNA binding sites in cell cytoplasm (*66*, *67*), which is estimated to greatly exceed both the protein-RNA affinities (likely tens of nanomolar for Gag and A3G binding to single strand RNAs (*42*, *68*, *69*)) and the protein concentrations (~1 µM) in DC z-scan measurements. The potential for protein-RNA binding equilibria or selective protein-RNA binding to influence the cortical partitioning effect may be explored with further studies utilizing DC z-scan.

FCS measurements were acquired in order to characterize protein mobility in the cytoplasm. Given that these data were acquired with the PSF focused near the middle of thick (>1.5 µm) cytoplasmic sections, the experimental estimates mainly report the mobility within the cytoplasm and not the mobility within the actin cortex. The diffusion time of RNA binding proteins revealed that large <*Δ*> values were associated with very low mobility (Fig. 6A), as expected for proteins that are present in large complexes. Slow diffusion of large sized objects in the cytoplasm has been previously reported (*14*, *17*, *70*, *71*), including mRNAs (*72*). Previous studies have suggested that this low cytoplasmic mobility may reflect a hindrance created by cytoskeletal elements (*15*, *16*, *18*, *19*, *62*, *73*, *74*) or by cytoplasmic crowding created due to ribosomes, organelles and proteins (*17*, *70*, *75*–*77*). Although the precise determinants for cytoplasmic mobility have not been fully characterized, existing literature provides extensive evidence that the cytoplasm cannot be described as a simple fluid (*12*, *53*, *75*, *78*), and it is generally agreed that particles in the range of 10 – 100nm show a size-dependent drop in cytoplasmic mobility much greater than that predicted by the Stokes-Einstein relation (*14*, *17*, *18*, *70*). In this study, a marked increase in A3G-EGFP mobility in cell-associated blebs (Fig. 6A) was observed. This suggests a role for the cytoskeleton in the mobility of large macromolecular complexes.

To capture the size dependence of RNP diffusion, an empirical hydrodynamic scaling model (Eq. 7) was used. This and similar models have been previously employed to describe diffusion in polymer solutions and in living cells (*53*, *54*). This model led to good agreement with our experimental data (Fig. 6A)

when combined with a relatively simple description of the size dependence of cortical partitioning (*50–52*) (Eq. 6). This result demonstrates the feasibility of a quantitative description of the actin cortical partitioning effect. The choice to model the partition coefficient as arising from the excluded volume due to spherical cavity (Eq. 6) was driven primarily by the simplicity of this approach. The excluded volume due to a mesh of randomly oriented fibers, which may provide a more realistic model of cortical actin, is expected to give similar results to Eq. 6 (*50*) at the expense of an additional free parameter.

This study presents data suggesting that large RNP complexes are disproportionately partitioned from the space immediately adjacent to the PM due to the presence of the dense cortical actin meshwork. In this phenomenon the physical properties of the cortical space appear to drive subcellular segregation of macromolecules in the absence of a clear boundary such as a membrane. Other instances of biomolecule compartmentalization in the absence of membranes have been recognized, such as that observed between P-bodies and the cytoplasm (*79*), and between nucleoli and the nucleoplasm (*80*). In such cases, the distinct physical properties of each subcellular compartment regulate their molecular content (*81*). Partitioning of large complexes from the cortical space is consistent with observations demonstrating that a highly orchestrated coupling between exocytic pathways and cortical actin polymerization is needed to facilitate passage of vesicles through the cortex when the actin fiber density is transiently lowered (*82*, *83*). Moreover, the cortical partitioning effect might hinder the replication of enveloped viruses, which target large macromolecular complexes to the PM as part of their assembly processes. In conclusion, new developments in DC z-scan microscopy have enabled the observation and characterization of an unexpected cortical partitioning effect that applies to large RNP complexes. A simple quantitative model was introduced to provide a rudimentary foundation for understanding the origins of this effect. The DC z-scan toolkit should be of interest to probe the spatial relation of biomolecules with other cellular structures as well as continue to provide additional insights into the function of the actin cortex.

Materials and Methods

Cell Culture and Plasmids

HeLa and U2OS (Numbers CCL-2 and HTB-96, American Type Culture Collection, Manassas, VA) cells were cultured in Dulbecco's modified Eagle's medium supplemented with 10% FBS (HyClone Laboratories, Logan, UT) at 37°C and 5% CO_2. Cells were plated at ~30% confluency into 8-well chambered slides ~24 h prior to measurement and transfected with vectors as indicated in the text ~16 h prior to measurement using

GenJet transfection reagent (SignaGen Laboratories, Fredrick, MD) according to the manufacturer's instructions. The cell growth medium was replaced with phosphate buffered saline immediately prior to measurement. All measurements were performed at room temperature.

HIV-1 Gag (*84*) was ligated into pEGFP-N1 (Clontech, Takara Bio, Mountain View, CA) to generate the HIV-1 Gag-EGFP vector. HIV-1 Gag^{G2A} -EGFP was made using the QuikChange XL Site-Directed Mutagenesis Kit (Stratagene, La Jolla, CA). $Venus_6$ was a gift from Steven Vogel (*85*) (Addgene plasmid # 27813; http://n2t.net/addgene:27813; RRID: Addgene_27813). mApple-Lifeact-7 (denoted Lifeact-mApple here) was a gift from Michael Davidson (Addgene plasmid # 54747; http://n2t.net/addgene:54747; RRID: Addgene_54747). All other vectors have been previously described: A3G-EGFP, $A3G^{C97A}$-EGFP, A3C-EGFP, A3A-EGFP (*44*); HIV-1 MA^{G2A}-EGFP (*20*); mCherry (*86*); EGFP-HRas (*21*); mCherry-RXR (*87*); GABARAP-EGFP (*88*).

Instrumentation

DC z-scans and fluorescence fluctuation spectroscopy (FFS) data were acquired on a Zeiss Axiovert 200 microscope modified for 2-photon excitation (*20*). Excitation light was provided by a femtosecond pulsed Ti:S laser (MaiTai or Tsunami models, Spectra Physics, Santa Clara, CA) operated at 1000 nm. This light was focused to a diffraction limited point by a water immersion objective (C-Apochromat, Zeiss, Oberkochen, Germany) with numerical aperture 1.2 and correction collar set according to the glass thickness of the sample holder. Emission light was collected by the same objective and separated from the excitation light by a dichroic filter (740DCSPXR, Chroma Technology, Bellows Falls, VT), then split into red and green detection channels by a low-pass dichroic (FF580-FDi01, Semrock, Rochester, NY). A 515/50nm band pass filter placed before the green channel detector eliminated Fresnel reflected mCherry emission light from the green channel. Emission light in each channel was detected by single photon counting hybrid photomultipliers (HPM-100-40, Becker and Hickl, Berlin, Germany), recorded by hardware (FastFLIM, ISS Inc., Champaign, IL or DPC-230, Becker and Hickl, Berlin, Germany), and saved for later analysis using routines written in IDL 8.6 (Harris Geospatial Solutions, Broomfield, CO).

Axial z-scans utilized a piezo stage (PZ2000, ASI, Eugene OR) driven by a voltage waveform from an arbitrary waveform generator (model 33250A, Agilent Technologies, Santa Clara, CA) to move the sample vertically across the two-photon point spread function (PSF). All z-scans were acquired by driving the piezo stage with a triangle waveform with a 10 s period and peak-to-peak displacement corresponding to 24 μm.

Each period contained two z-scans: the first z-scan passed upward through the cell and the second passed downward through the cell. Each z-scan covered a 24 μm range.

XY scanning of the PSF for acquisition of two-photon images was provided by a galvanometer scan head (Yanus IV, FEI Deutschland GmbH, Planegg, Germany) aligned in the two-photon excitation path. XY positioning was driven by a DAC card (3-axis, ISS Inc., Champaign, IL) controlled by SimFCS software (version 3; G-SOFT Inc., Champaign, IL). All z-scans were acquired within 24 μm of the XY scan field center.

Z-scan modeling

The single-channel (SC) z-scan fluorescence intensity profile $F(z)$ is determined by the convolution of the axial concentration profile $c(z)$ of the fluorescently-tagged protein and the radially integrated point spread function (RIPSF) of the two-photon instrument as modeled in (*22*, *32*),

$$F(z) = \lambda (c * \mathrm{RIPSF})(z), \qquad 9$$

where λ is the brightness of the fluorescence tag. Evaluation of Eq. 9 for different concentration profiles $c(z)$ gives rise to an alternative formulation with a fluorescence amplitude f and a function $\mathrm{v}(z)$ describing the shape of the concentration profile (*32*),

$$F(z) = f\,\mathrm{v}(z). \qquad 10$$

The axially integrated concentration $A = \int c(z)\,dz$ and the axially integrated fluorescence $\Lambda = \int F(z)\,dz$ are related according to Eq. 9 by

$$\Lambda = \eta A \qquad 11$$

with the constant $\eta = \lambda \int \mathrm{RIPSF}(z)\,dz$.

Z-scan and FFS acquisition in live cells

Cells were selected by verifying the desired expression levels for the mCherry and EGFP labeled constructs using 1-photon epi illumination provided by a mercury lamp and using an EGFP/mCherry filter set. Points within cells for z-scan and FFS data collection were chosen where the fluorescence appeared locally (~3 μm

radius) uniform as visualized in epi illumination and where a cell lacked nearby internal structures when visualized by using transmitted light. For data acquisition, the microscope was switched to two-photon mode and the excitation volume was focused to the middle of the cell. In most instances, 60 s of z-scan data acquisition was followed by an optional 60 s of FFS data acquisition at up to 4 unique locations within each cell. Z-scan acquisition times at a given location were lengthened to a maximum of 10 min in dim samples or where increased statistical precision was desired.

Effective diffusion coefficient

The effective diffusion coefficient was calculated as (*89*) $D_{eff} = \omega_0^2 / (8\tau_D)$, where ω_0^2 is the $1/e^2$ radial beam waist of the 2-photon excitation light focus and τ_D was estimated by fitting the log-averaged autocorrelation of photon counts $G(\tau)$ to $G_{2D}(\tau) = G_0 / (1 + (\tau/\tau_D))^{-1} + G_{offset}$. FCS data quality control was performed by redacting data where G_{offset} showed significantly negative values or where τ_D indicated by the fit was >50% higher than the time at which the correlation amplitude reached half its initial value.

Modeling of DC z-scan intensity profiles

The DC fluorescence intensity $\mathbf{F}^{\mathbf{G}}(z)$ of a z-scan intensity profile of EGFP (G)-labeled protein through a series of horizontal layers, each containing a uniform concentration of labels, is described by (*20–22*)

$$\mathbf{F}^{\mathbf{G}}(z) = \sum_i \mathbf{f}_i^{\mathbf{G}} \cdot \mathrm{v}\left(z; a_i^{\mathrm{G}}, b_i^{\mathrm{G}}\right) = \boldsymbol{\alpha}^{\mathbf{G}} \sum_i f_i^{\mathrm{G}} \cdot \mathrm{v}\left(z; a_i^{\mathrm{G}}, b_i^{\mathrm{G}}\right) , \qquad 12$$

where f_i^{G} and $\mathrm{v}\left(z, a_i^{\mathrm{G}}, b_i^{\mathrm{G}}\right)$ are the fluorescence amplitude and shape function associated with the *i*-th layer. The shape function $\mathrm{v}\left(z, a_i^{\mathrm{G}}, b_i^{\mathrm{G}}\right)$ characterizes a uniform slab or S layer starting at $z = a_i^{\mathrm{G}}$ and ending at $z = b_i^{\mathrm{G}}$, while $\mathrm{v}\left(z, a_i^{\mathrm{G}}, a_i^{\mathrm{G}}\right)$ defines an infinitesimally thin or δ layer located at $z = a_i^{\mathrm{G}}$ (*20–22*). Vector notation is used to describe properties of the green (g) and red (r) channel, i.e. $\mathbf{F}^{\mathbf{G}}(z) = \left(F_g^{\mathrm{G}}(z), F_r^{\mathrm{G}}(z)\right)$ and $\mathbf{f}_i^{\mathbf{G}} = \left(f_{i,g}^{\mathrm{G}}, f_{i,r}^{\mathrm{G}}\right)$. The broad emission spectrum of EGFP is split at the dichroic mirror, resulting in identical shapes of the z-scan profile in both channels. Their intensity ratio is specified by the crosstalk vector $\boldsymbol{\alpha}^{\mathbf{G}}$, which is defined by $\mathbf{f}_i^{\mathbf{G}} = \boldsymbol{\alpha}^{\mathbf{G}} f_i^{\mathrm{G}}$, where $f_i^{\mathrm{G}} = f_{i,g}^{\mathrm{G}} + f_{i,r}^{\mathrm{G}}$ is the sum

amplitude of both channels. Similarly, the DC z-scan intensity profiles of the red fluorescent protein mCherry (CH) are given by

$$\mathbf{F}^{\mathbf{CH}}(z) = \sum_i \mathbf{f}_i^{\mathbf{CH}} \cdot \mathrm{v}\left(z; a_i^{\mathrm{CH}}, b_i^{\mathrm{CH}}\right) = \boldsymbol{\alpha}^{\mathbf{CH}} \sum_i f_i^{\mathrm{CH}} \cdot \mathrm{v}\left(z; a_i^{\mathrm{CH}}, b_i^{\mathrm{CH}}\right), \qquad 13$$

and the presence of both proteins is described by the sum of Eqs. 12 and 13,

$$\mathbf{F}(z) = \mathbf{F}^{\mathbf{G}}(z) + \mathbf{F}^{\mathbf{CH}}(z). \qquad 14$$

Only a few scan geometries are of interest for modeling of the data in this study. The first uses a single slab layer to describe the distribution of EGFP (X = G) and mCherry (X = CH) labeled species,

$$\mathbf{F}_{\mathbf{S}}^{\mathbf{X}}(z) = \boldsymbol{\alpha}^{\mathbf{X}} f^{\mathrm{X}}\, \mathrm{v}\left(z; a^{\mathrm{X}}, b^{\mathrm{X}}\right), \qquad 15$$

as illustrated in Fig. 1A. The second geometry consists of a delta layer followed by a slab layer and another delta layer, which is referred to as (δSδ) layer model (*20–22*). This model was introduced to describe peripheral membrane proteins with the δ layers representing the top and bottom plasma membrane, while the S layer describes the cytoplasmic space (*21*). The DC z-scan (δSδ) model is given by

$$\mathbf{F}_{\boldsymbol{\delta}\mathbf{S}\boldsymbol{\delta}}^{\mathbf{X}}(z) = \boldsymbol{\alpha}^{\mathbf{X}}\left(f_{\mathrm{B}}^{\mathrm{X}} \cdot \mathrm{v}\left(z; a^{\mathrm{X}}, a^{\mathrm{X}}\right) + f_{\mathrm{Cy}}^{\mathrm{X}} \cdot \mathrm{v}\left(z; a^{\mathrm{X}}, b^{\mathrm{X}}\right) + f_{\mathrm{T}}^{\mathrm{X}} \cdot \mathrm{v}\left(z; b^{\mathrm{X}}, b^{\mathrm{X}}\right)\right), \qquad 16$$

where a^{X} and b^{X} mark the axial height of the bottom (B) and top (T) membrane (see Fig. 1G). The fluorescence amplitudes of the B, T and cytoplasmic (Cy) layer are given by $f_{\mathrm{B}}^{\mathrm{X}}$, $f_{\mathrm{T}}^{\mathrm{X}}$, and $f_{\mathrm{Cy}}^{\mathrm{X}}$.

The DC z-scan of cells co-expressing EGFP and mCherry labeled proteins is described by a superposition of their individual profiles (Eq. 14). The notation X^G-Y^{CH} was used to describe a model where the z-scan intensity of the EGFP-labeled protein is described by the X profile, while the z-scan intensity of the mCherry-labeled protein is given by the Y profile,

$$\mathbf{F}_{\mathbf{X\text{-}Y}}(z) = \mathbf{F}_{\mathbf{X}}^{\mathbf{G}}(z) + \mathbf{F}_{\mathbf{Y}}^{\mathbf{CH}}(z), \qquad 17$$

where X and Y denote either the S or δSδ model (Eqs. 15 and 16). For example, the S^G-S^{CH} model is based on independent slab layers for the EGFP and mCherry-labeled proteins, while the $\delta S\delta^G$-S^{CH} model uses the (δSδ) model for the EGFP label and a slab layer for mCherry.

Determining cell thickness from the z-scan intensity profile

For a cell section that is thick with respect to the RIPSF width, a direct fit of the intensity profile to a slab model (Eq. 15) determines the cell thickness by $L_{cell} = b^{CH} - a^{CH}$. For cell sections that are thin with respect to the RIPSF, cell thickness cannot be reliably determined from fitting to a slab model (*32*). However, because the fluorescent protein mCherry is distributed uniformly throughout the cell interior, its z-scan intensity provides a measure of local cell thickness L_{cell}. In this manner the cell thickness in thin sections can be determined from the integrated fluorescence Λ^{CH} of the intensity profile. Λ^{CH} is proportional to the integrated concentration area A^{CH} (Eq. 11), which is $L_{cell}c^{CH}$ for the slab geometry, where the mCherry concentration c^{CH} is assumed constant throughout the cell. Thus, the ratio of the integrated intensity profiles from a thick and a thin section measured in the same cell equals their thickness ratio, $\Lambda^{CH}_{thin} / \Lambda^{CH}_{thick} = L_{cell,thin} / L_{cell,thick}$, which was used to determine the thickness of thin cell sections. Although previous work (*32*) defined the cutoff between thick and thin cell lections as L_{cell} = 0.5 μm, a more conservative value of 1.5 μm was used in this study to improve the precision of length measurements .

Production of PM blebs

Bulges along the plasma membrane (i.e., blebs) were induced along the PM of cultured HeLa cells by adding 10-15% ethanol (*23*) to the cell growth medium and incubating for ~15 min at 37ºC and 5% CO_2. The ethanol-treated cells were subsequently analyzed by transmitted light microscopy to assess the number and size of blebs with the goal of producing blebs with ~5μm diameter in sufficient quantity for measurement. If insufficient blebbing was observed, cells were returned to the incubator for ~10 min before re-checking. Once sufficient blebbing was obtained, the growth medium with ethanol was exchanged by PBS containing ethanol immediately before measurement.

SYTO RNASelect cell stain

Live cells were stained with SYTO RNASelect (Thermo Fisher Scientific, Waltham, MA) by diluting the stock dye 1000x (5 μM final concentration) into the cell culture medium followed by incubation for 1 h at 37 ºC and 5% CO_2. For measurement, the growth medium with SYTO RNASelect was replaced by PBS containing the same concentration of the dye.

Z-scan redaction and statistical analysis

Despite the selection of scan locations as described earlier, some of the measured z-scan intensity profiles were not adequately described by our fit model. This was attributed to scans that inadvertently passed through complex intracellular structures. Since these structures are not captured by the model framework, the spatial autocorrelation of the normalized residual from the fit was calculated to identify patterns that are indicative of the presence of extraneous cellular features not described by the fit model. Scans with a correlation amplitude exceeding a threshold value were removed. Furthermore, z-scan measurements of the cortex thickness were selected to have a cell thickness $L_{cell} \geq 2.5$ µm and a membrane fraction (*22*) $m \geq 0.5$ in order to ensure the absence of biases in the fitted values as supported by our study using simulated DC z-scans (Fig. S1). Quality control for the z-scan fits of cortex thickness was provided by averaging the normalized residuals within ±1 µm of the fitted PM locations. Scans where these averaged residuals exceeded 2.5 in either the red or green channel were redacted.

A typical z-scan acquisition at a single location contained 12 repeated scans, which were fit individually, yielding 12 estimates of each parameter of interest. This set of parameters served to calculate the average effective depletion length $\overline{\Delta}_i$ and its standard deviation σ_i at the *i*-th z-scan location. Multiple measurement locations were summarized using the weighted average $\langle \Delta \rangle$ over all locations with $1/\sigma_i^2$ as weight. The uncertainty in the weighted average was computed using the dispersion corrected standard error of the mean (SEM),

$$SEM^2 = \sigma_{we}^2 \left(\frac{1}{n-1} \sum_i \frac{(\overline{\Delta}_i - \langle \Delta \rangle)^2}{\sigma_i^2} \right) \qquad 18$$

where σ_{we}^2 is the variance of the weighted average. Since it was observed that $\langle \Delta \rangle$ at the top (T) and bottom (B) PM interfaces are in agreement ($\langle \Delta^T \rangle \approx \langle \Delta^B \rangle$), data from both interfaces were grouped together when calculating $\langle \Delta \rangle$. This is indicated by dropping the *T* and *B* superscript.

Simulations of z-scan traces

Simulated DC z-scan traces were obtained following a previously described procedure (*20*) to evaluate models and estimate the statistical uncertainty in DC z-scan fit results. Simulated DC z-scan traces were fit using the same algorithms that were applied to experimental data. All data derived from simulations represent the average result from fits of n = 1000 z-scan traces.

References

1. P. Chugh, E. K. Paluch, The actin cortex at a glance. *J Cell Sci*. **131** (2018), doi:10.1242/jcs.186254.

2. A. Kusumi, T. K. Fujiwara, R. Chadda, M. Xie, T. A. Tsunoyama, Z. Kalay, R. S. Kasai, K. G. N. Suzuki, Dynamic organizing principles of the plasma membrane that regulate signal transduction: commemorating the fortieth anniversary of Singer and Nicolson's fluid-mosaic model. *Annu Rev Cell Dev Biol*. **28**, 215–250 (2012).

3. M. D. Blower, Molecular insights into intracellular RNA localization. *Int Rev Cell Mol Biol*. **302**, 1–39 (2013).

4. C. Medioni, K. Mowry, F. Besse, Principles and roles of mRNA localization in animal development. *Development*. **139**, 3263–3276 (2012).

5. E. Lécuyer, H. Yoshida, N. Parthasarathy, C. Alm, T. Babak, T. Cerovina, T. R. Hughes, P. Tomancak, H. M. Krause, Global analysis of mRNA localization reveals a prominent role in organizing cellular architecture and function. *Cell*. **131**, 174–187 (2007).

6. A. Gopal, Z. H. Zhou, C. M. Knobler, W. M. Gelbart, Visualizing large RNA molecules in solution. *RNA*. **18**, 284–299 (2012).

7. A. Borodavka, S. W. Singaram, P. G. Stockley, W. M. Gelbart, A. Ben-Shaul, R. Tuma, Sizes of Long RNA Molecules Are Determined by the Branching Patterns of Their Secondary Structures. *Biophys J*. **111**, 2077–2085 (2016).

8. S. S. Sommer, J. E. Cohen, The size distributions of proteins, mRNA, and nuclear RNA. *J Mol Evol*. **15**, 37–57 (1980).

9. I. Legnini, J. Alles, N. Karaiskos, S. Ayoub, N. Rajewsky, FLAM-seq: full-length mRNA sequencing reveals principles of poly(A) tail length control. *Nat Methods*. **16**, 879–886 (2019).

10. M. F. Tam, J. A. Dodd, W. E. Hill, Physical characteristics of 16 S rRNA under reconstitution conditions. *J Biol Chem*. **256**, 6430–6434 (1981).

11. A. Verschoor, J. Frank, Three-dimensional structure of the mammalian cytoplasmic ribosome. *J Mol Biol*. **214**, 737–749 (1990).

12. G. T. Charras, T. J. Mitchison, L. Mahadevan, Animal cell hydraulics. *J Cell Sci*. **122**, 3233–3241 (2009).

13. E. Moeendarbary, L. Valon, M. Fritzsche, A. R. Harris, D. A. Moulding, A. J. Thrasher, E. Stride, L. Mahadevan, G. T. Charras, The cytoplasm of living cells behaves as a poroelastic material. *Nat Mater*. **12**, 253–261 (2013).

14. K. Luby-Phelps, P. E. Castle, D. L. Taylor, F. Lanni, Hindered diffusion of inert tracer particles in the cytoplasm of mouse 3T3 cells. *Proc Natl Acad Sci U S A*. **84**, 4910–4913 (1987).

15. K. Luby-Phelps, D. L. Taylor, Subcellular compartmentalization by local differentiation of cytoplasmic structure. *Cell Motil Cytoskeleton*. **10**, 28–37 (1988).

16. L. Hou, F. Lanni, K. Luby-Phelps, Tracer diffusion in F-actin and Ficoll mixtures. Toward a model for cytoplasm. *Biophys J*. **58**, 31–43 (1990).

17. G. L. Lukacs, P. Haggie, O. Seksek, D. Lechardeur, N. Freedman, A. S. Verkman, Size-dependent DNA mobility in cytoplasm and nucleus. *J Biol Chem*. **275**, 1625–1629 (2000).

18. E. Dauty, A. S. Verkman, Actin cytoskeleton as the principal determinant of size-dependent DNA mobility in cytoplasm: a new barrier for non-viral gene delivery. *J Biol Chem*. **280**, 7823–7828 (2005).

19. K. Luby-Phelps, Effect of cytoarchitecture on the transport and localization of protein synthetic machinery. *Journal of Cellular Biochemistry*. **52**, 140–147 (1993).

20. I. Angert, S. R. Karuka, J. Hennen, Y. Chen, J. P. Albanesi, L. M. Mansky, J. D. Mueller, Sensitive Detection of Protein Binding to the Plasma Membrane with Dual-Color Z-Scan Fluorescence. *Biophys J*. **118**, 281–293 (2020).

21. E. M. Smith, P. J. Macdonald, Y. Chen, J. D. Mueller, Quantifying protein-protein interactions of peripheral membrane proteins by fluorescence brightness analysis. *Biophys J*. **107**, 66–75 (2014).

22. E. M. Smith, J. Hennen, Y. Chen, J. D. Mueller, Z-scan fluorescence profile deconvolution of cytosolic and membrane-associated protein populations. *Anal Biochem*. **480**, 11–20 (2015).

23. S. Saha, I.-H. Lee, A. Polley, J. T. Groves, M. Rao, S. Mayor, Diffusion of GPI-anchored proteins is influenced by the activity of dynamic cortical actin. *Mol Biol Cell*. **26**, 4033–4045 (2015).

24. R. E. Scott, R. G. Perkins, M. A. Zschunke, B. J. Hoerl, P. B. Maercklein, Plasma membrane vesiculation in 3T3 and SV3T3 cells. I. Morphological and biochemical characterization. *J Cell Sci*. **35**, 229–243 (1979).

25. T. Baumgart, A. T. Hammond, P. Sengupta, S. T. Hess, D. A. Holowka, B. A. Baird, W. W. Webb, Large-scale fluid/fluid phase separation of proteins and lipids in giant plasma membrane vesicles. *Proc Natl Acad Sci U S A*. **104**, 3165–3170 (2007).

26. F. Schneider, D. Waithe, M. P. Clausen, S. Galiani, T. Koller, G. Ozhan, C. Eggeling, E. Sezgin, Diffusion of lipids and GPI-anchored proteins in actin-free plasma membrane vesicles measured by STED-FCS. *Mol Biol Cell*. **28**, 1507–1518 (2017).

27. T. M. Svitkina, Actin Cell Cortex: Structure and Molecular Organization. *Trends Cell Biol*. **30**, 556–565 (2020).

28. N. Morone, T. Fujiwara, K. Murase, R. S. Kasai, H. Ike, S. Yuasa, J. Usukura, A. Kusumi, Three-dimensional reconstruction of the membrane skeleton at the plasma membrane interface by electron tomography. *J Cell Biol*. **174**, 851–862 (2006).

29. P. Chugh, A. G. Clark, M. B. Smith, D. A. D. Cassani, K. Dierkes, A. Ragab, P. P. Roux, G. Charras, G. Salbreux, E. K. Paluch, Actin cortex architecture regulates cell surface tension. *Nat Cell Biol*. **19**, 689–697 (2017).

30. A. G. Clark, K. Dierkes, E. K. Paluch, Monitoring actin cortex thickness in live cells. *Biophys J*. **105**, 570–580 (2013).

31. J. Riedl, A. H. Crevenna, K. Kessenbrock, J. H. Yu, D. Neukirchen, M. Bista, F. Bradke, D. Jenne, T. A. Holak, Z. Werb, M. Sixt, R. Wedlich-Soldner, Lifeact: a versatile marker to visualize F-actin. *Nat Methods*. **5**, 605–607 (2008).

32. P. J. Macdonald, Y. Chen, X. Wang, Y. Chen, J. D. Mueller, Brightness analysis by Z-scan fluorescence fluctuation spectroscopy for the study of protein interactions within living cells. *Biophys J*. **99**, 979–988 (2010).

33. P. R. Tedbury, E. O. Freed, HIV-1 gag: an emerging target for antiretroviral therapy. *Curr Top Microbiol Immunol*. **389**, 171–201 (2015).

34. J. G. Levin, J. Guo, I. Rouzina, K. Musier-Forsyth, Nucleic acid chaperone activity of HIV-1 nucleocapsid protein: critical role in reverse transcription and molecular mechanism. *Prog Nucleic Acid Res Mol Biol*. **80**, 217–286 (2005).

35. R. N. De Guzman, Z. R. Wu, C. C. Stalling, L. Pappalardo, P. N. Borer, M. F. Summers, Structure of the HIV-1 nucleocapsid protein bound to the SL3 psi-RNA recognition element. *Science*. **279**, 384–388 (1998).

36. A. Rein, Nucleic acid chaperone activity of retroviral Gag proteins. *RNA Biol*. **7**, 700–705 (2010).

37. V. Chukkapalli, S. J. Oh, A. Ono, Opposing mechanisms involving RNA and lipids regulate HIV-1 Gag membrane binding through the highly basic region of the matrix domain. *Proc Natl Acad Sci U S A*. **107**, 1600–1605 (2010).

38. P. Purohit, S. Dupont, M. Stevenson, M. R. Green, Sequence-specific interaction between HIV-1 matrix protein and viral genomic RNA revealed by in vitro genetic selection. *RNA*. **7**, 576–584 (2001).

39. D. Thornhill, B. Olety, A. Ono, Relationships between MA-RNA Binding in Cells and Suppression of HIV-1 Gag Mislocalization to Intracellular Membranes. *J Virol*. **93** (2019), doi:10.1128/JVI.00756-19.

40. C. R. Gaines, E. Tkacik, A. Rivera-Oven, P. Somani, A. Achimovich, T. Alabi, A. Zhu, N. Getachew, A. L. Yang, M. McDonough, T. Hawkins, Z. Spadaro, M. F. Summers, HIV-1 Matrix Protein Interactions with tRNA: Implications for Membrane Targeting. *J Mol Biol*. **430**, 2113–2127 (2018).

41. S. B. Kutluay, T. Zang, D. Blanco-Melo, C. Powell, D. Jannain, M. Errando, P. D. Bieniasz, Global changes in the RNA binding specificity of HIV-1 gag regulate virion genesis. *Cell*. **159**, 1096–1109 (2014).

42. Y. Iwatani, H. Takeuchi, K. Strebel, J. G. Levin, Biochemical activities of highly purified, catalytically active human APOBEC3G: correlation with antiviral effect. *J Virol*. **80**, 5992–6002 (2006).

43. Y. N. Friew, V. Boyko, W.-S. Hu, V. K. Pathak, Intracellular interactions between APOBEC3G, RNA, and HIV-1 Gag: APOBEC3G multimerization is dependent on its association with RNA. *Retrovirology*. **6**, 56 (2009).

44. J. Li, Y. Chen, M. Li, M. A. Carpenter, R. M. McDougle, E. M. Luengas, P. J. Macdonald, R. S. Harris, J. D. Mueller, APOBEC3 multimerization correlates with HIV-1 packaging and restriction activity in living cells. *J Mol Biol*. **426**, 1296–1307 (2014).

45. E. S. Svarovskaia, H. Xu, J. L. Mbisa, R. Barr, R. J. Gorelick, A. Ono, E. O. Freed, W.-S. Hu, V. K. Pathak, Human apolipoprotein B mRNA-editing enzyme-catalytic polypeptide-like 3G (APOBEC3G) is incorporated into HIV-1 virions through interactions with viral and nonviral RNAs. *J Biol Chem*. **279**, 35822–35828 (2004).

46. A. Burnett, P. Spearman, APOBEC3G multimers are recruited to the plasma membrane for packaging into human immunodeficiency virus type 1 virus-like particles in an RNA-dependent process requiring the NC basic linker. *J Virol*. **81**, 5000–5013 (2007).

47. B. R. Cullen, Role and mechanism of action of the APOBEC3 family of antiretroviral resistance factors. *J Virol*. **80**, 1067–1076 (2006).

48. J. S. Albin, R. S. Harris, Interactions of host APOBEC3 restriction factors with HIV-1 in vivo: implications for therapeutics. *Expert Rev Mol Med*. **12**, e4 (2010).

49. J. F. Hultquist, J. A. Lengyel, E. W. Refsland, R. S. LaRue, L. Lackey, W. L. Brown, R. S. Harris, Human and rhesus APOBEC3D, APOBEC3F, APOBEC3G, and APOBEC3H demonstrate a conserved capacity to restrict Vif-deficient HIV-1. *J Virol*. **85**, 11220–11234 (2011).

50. L. W. Janson, K. Ragsdale, K. Luby-Phelps, Mechanism and size cutoff for steric exclusion from actin-rich cytoplasmic domains. *Biophys J*. **71**, 1228–1234 (1996).

51. A. P. Minton, Confinement as a determinant of macromolecular structure and reactivity. *Biophys J*. **63**, 1090–1100 (1992).

52. J. C. Giddings, E. Kucera, C. P. Russell, M. N. Myers, Statistical theory for the equilibrium distribution of rigid molecules in inert porous networks. Exclusion chromatography. *J. Phys. Chem.* **72**, 4397–4408 (1968).

53. T. Kalwarczyk, N. Ziebacz, A. Bielejewska, E. Zaboklicka, K. Koynov, J. Szymański, A. Wilk, A. Patkowski, J. Gapiński, H.-J. Butt, R. Hołyst, Comparative analysis of viscosity of

complex liquids and cytoplasm of mammalian cells at the nanoscale. *Nano Lett*. **11**, 2157–2163 (2011).

54. R. Holyst, A. Bielejewska, J. Szymański, A. Wilk, A. Patkowski, J. Gapiński, A. Zywociński, T. Kalwarczyk, E. Kalwarczyk, M. Tabaka, N. Ziebacz, S. A. Wieczorek, Scaling form of viscosity at all length-scales in poly(ethylene glycol) solutions studied by fluorescence correlation spectroscopy and capillary electrophoresis. *Phys Chem Chem Phys*. **11**, 9025–9032 (2009).

55. L. Xiang, K. Chen, R. Yan, W. Li, K. Xu, Single-molecule displacement mapping unveils nanoscale heterogeneities in intracellular diffusivity. *Nat Methods*. **17**, 524–530 (2020).

56. T. P. Stossel, P. A. Janmey, K. S. Zaner, in *Cytomechanics: The Mechanical Basis of Cell Form and Structure*, J. Bereiter-Hahn, O. R. Anderson, W.-E. Reif, Eds. (Springer, Berlin, Heidelberg, 1987; https://doi.org/10.1007/978-3-642-72863-1_9), pp. 131–153.

57. J.-F. Joanny, J. Prost, Active gels as a description of the actin-myosin cytoskeleton. *HFSP J*. **3**, 94–104 (2009).

58. T. C. Laurent, J. Killander, A theory of gel filtration and its exeperimental verification. *Journal of Chromatography A*. **14**, 317–330 (1964).

59. K. C. Duong-Ly, S. B. Gabelli, Gel filtration chromatography (size exclusion chromatography) of proteins. *Methods Enzymol*. **541**, 105–114 (2014).

60. T. Kaur, I. Alshareedah, W. Wang, J. Ngo, M. M. Moosa, P. R. Banerjee, Molecular Crowding Tunes Material States of Ribonucleoprotein Condensates. *Biomolecules*. **9** (2019), doi:10.3390/biom9020071.

61. A. A. M. André, E. Spruijt, Liquid-Liquid Phase Separation in Crowded Environments. *Int J Mol Sci*. **21** (2020), doi:10.3390/ijms21165908.

62. D. W. Provance, A. McDowall, M. Marko, K. Luby-Phelps, Cytoarchitecture of size-excluding compartments in living cells. *J Cell Sci*. **106 (Pt 2)**, 565–577 (1993).

63. K. Luby-Phelps, D. L. Taylor, F. Lanni, Probing the structure of cytoplasm. *J Cell Biol*. **102**, 2015–2022 (1986).

64. R. Kumar, S. Saha, B. Sinha, Cell spread area and traction forces determine myosin-II-based cortex thickness regulation. *Biochim Biophys Acta Mol Cell Res*. **1866**, 118516 (2019).

65. T. M. Svitkina, A. A. Shevelev, A. D. Bershadsky, V. I. Gelfand, Cytoskeleton of mouse embryo fibroblasts. Electron microscopy of platinum replicas. *Eur J Cell Biol*. **34**, 64–74 (1984).

66. F. Feijó Delgado, N. Cermak, V. C. Hecht, S. Son, Y. Li, S. M. Knudsen, S. Olcum, J. M. Higgins, J. Chen, W. H. Grover, S. R. Manalis, Intracellular water exchange for measuring the dry mass, water mass and changes in chemical composition of living cells. *PLoS One*. **8**, e67590 (2013).

67. M. A. Urbaneja, B. P. Kane, D. G. Johnson, R. J. Gorelick, L. E. Henderson, J. R. Casas-Finet, Binding properties of the human immunodeficiency virus type 1 nucleocapsid protein p7 to a model RNA: elucidation of the structural determinants for function. *J Mol Biol*. **287**, 59–75 (1999).

68. W. Ouyang, S. Okaine, M. P. McPike, Y. Lin, P. N. Borer, Probing the RNA binding surface of the HIV-1 nucleocapsid protein by site-directed mutagenesis. *Biochemistry*. **52**, 3358–3368 (2013).

69. M. Comas-Garcia, S. A. Datta, L. Baker, R. Varma, P. R. Gudla, A. Rein, Dissection of specific binding of HIV-1 Gag to the “packaging signal” in viral RNA. *Elife*. **6** (2017), doi:10.7554/eLife.27055.

70. M. Delarue, G. P. Brittingham, S. Pfeffer, I. V. Surovtsev, S. Pinglay, K. J. Kennedy, M. Schaffer, J. I. Gutierrez, D. Sang, G. Poterewicz, J. K. Chung, J. M. Plitzko, J. T. Groves, C. Jacobs-Wagner, B. D. Engel, L. J. Holt, mTORC1 Controls Phase Separation and the Biophysical Properties of the Cytoplasm by Tuning Crowding. *Cell*. **174**, 338-349.e20 (2018).

71. K. Kwapiszewska, K. Szczepański, T. Kalwarczyk, B. Michalska, P. Patalas-Krawczyk, J. Szymański, T. Andryszewski, M. Iwan, J. Duszyński, R. Hołyst, Nanoscale Viscosity of Cytoplasm Is Conserved in Human Cell Lines. *J Phys Chem Lett*. **11**, 6914–6920 (2020).

72. J. Chen, D. Grunwald, L. Sardo, A. Galli, S. Plisov, O. A. Nikolaitchik, D. Chen, S. Lockett, D. R. Larson, V. K. Pathak, W.-S. Hu, Cytoplasmic HIV-1 RNA is mainly transported by diffusion in the presence or absence of Gag protein. *Proc Natl Acad Sci U S A*. **111**, E5205-5213 (2014).

73. J. J. Blum, G. Lawler, M. Reed, I. Shin, Effect of cytoskeletal geometry on intracellular diffusion. *Biophys J*. **56**, 995–1005 (1989).

74. K. Luby-Phelps, F. Lanni, D. L. Taylor, The submicroscopic properties of cytoplasm as a determinant of cellular function. *Annu Rev Biophys Biophys Chem*. **17**, 369–396 (1988).

75. D. S. Banks, C. Fradin, Anomalous diffusion of proteins due to molecular crowding. *Biophys J*. **89**, 2960–2971 (2005).

76. A. Miermont, F. Waharte, S. Hu, M. N. McClean, S. Bottani, S. Léon, P. Hersen, Severe osmotic compression triggers a slowdown of intracellular signaling, which can be explained by molecular crowding. *Proc Natl Acad Sci U S A*. **110**, 5725–5730 (2013).

77. M. Weiss, M. Elsner, F. Kartberg, T. Nilsson, Anomalous subdiffusion is a measure for cytoplasmic crowding in living cells. *Biophys J*. **87**, 3518–3524 (2004).

78. C. I. Lacayo, J. A. Theriot, Listeria monocytogenes actin-based motility varies depending on subcellular location: a kinematic probe for cytoarchitecture. *Mol Biol Cell*. **15**, 2164–2175 (2004).

79. J.-Y. Youn, B. J. A. Dyakov, J. Zhang, J. D. R. Knight, R. M. Vernon, J. D. Forman-Kay, A.-C. Gingras, Properties of Stress Granule and P-Body Proteomes. *Mol Cell*. **76**, 286–294 (2019).

80. A. A. Hyman, C. A. Weber, F. Jülicher, Liquid-liquid phase separation in biology. *Annu Rev Cell Dev Biol*. **30**, 39–58 (2014).

81. L.-P. Bergeron-Sandoval, N. Safaee, S. W. Michnick, Mechanisms and Consequences of Macromolecular Phase Separation. *Cell*. **165**, 1067–1079 (2016).

82. R. Wollman, T. Meyer, Coordinated oscillations in cortical actin and Ca2+ correlate with cycles of vesicle secretion. *Nat Cell Biol*. **14**, 1261–1269 (2012).

83. P. Li, A. T. Bademosi, J. Luo, F. A. Meunier, Actin Remodeling in Regulated Exocytosis: Toward a Mesoscopic View. *Trends Cell Biol*. **28**, 685–697 (2018).

84. A. Derdowski, L. Ding, P. Spearman, A novel fluorescence resonance energy transfer assay demonstrates that the human immunodeficiency virus type 1 Pr55Gag I domain mediates Gag-Gag interactions. *J Virol*. **78**, 1230–1242 (2004).

85. C. Thaler, S. V. Koushik, H. L. Puhl, P. S. Blank, S. S. Vogel, Structural rearrangement of CaMKIIalpha catalytic domains encodes activation. *Proc Natl Acad Sci U S A*. **106**, 6369–6374 (2009).

86. B. Wu, Y. Chen, J. D. Müller, Fluorescence fluctuation spectroscopy of mCherry in living cells. *Biophys J*. **96**, 2391–2404 (2009).

87. B. Wu, Y. Chen, J. D. Müller, Heterospecies partition analysis reveals binding curve and stoichiometry of protein interactions in living cells. *Proc Natl Acad Sci U S A*. **107**, 4117–4122 (2010).

88. Y. Chen, H.-Q. Sun, J. P. Eichorst, J. P. Albanesi, H. Yin, J. D. Mueller, Comobility of GABARAP and Phosphatidylinositol 4-Kinase 2A on Cytoplasmic Vesicles. *Biochemistry*. **57**, 3556–3559 (2018).

89. J. D. Müller, Y. Chen, E. Gratton, Fluorescence correlation spectroscopy. *Methods Enzymol*. **361**, 69–92 (2003).

Acknowledgments

Non-author contributions: The authors thank Yan Chen for help with logistics and experiment planning.

Author contributions: CIA, JDM, and SRK developed the dual color z-scan method. CIA and SRK performed experiments and acquired the data. LMM helped interpret the data and guide the project. CIA and JDM wrote analysis code, performed data analysis, and drafted the manuscript. All authors reviewed and revised the manuscript.

Funding: This work was supported by NIH grants GM064589, GM124279 and GM098550. C. I. A. was supported by NIH T32 AI083196

Competing interests: The authors declare that they have no financial or other competing interests.

Data and materials availability: The raw data and code necessary to perform the analyses will be made available through the Dryad data repository.

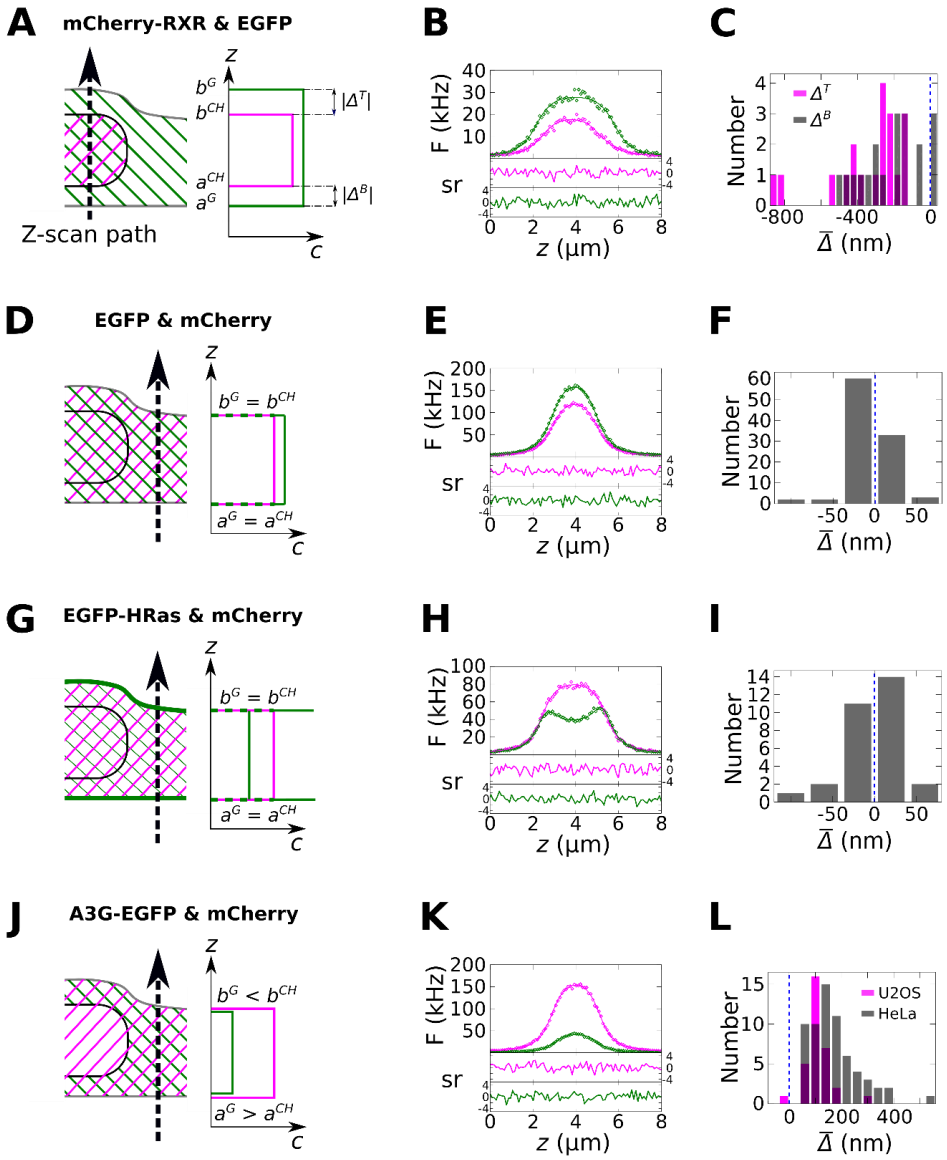

Fig. 1: DC z-scans in living cells. The z-scan trajectory through the cell is depicted in the cartoons along with crosshatched regions indicating the subcellular localization of the EGFP- and mCherry-labeled proteins (A, D, G, J, left panel) together with the concentration profile indicated by z-scan fitting for the EGFP (green lines) and mCherry (magenta lines) protein species (A, D, G, J, right panel). B, E, H, K) Fits (solid lines) of representative z-scan intensity traces of the green (green diamonds) and red (magenta diamonds) detection channel are shown along with their normalized residuals *sr*. The cell edge locations a^G, b^G, a^{CH}, b^{CH} extracted from the fits determine the vertical distance Δ separating the EGFP- and mCherry-labeled slab edges in each z-scan. C, F, I, L) Histograms of $\bar{\Delta}$ from repeated z-scan experiments in many cells. Experiments with different EGFP- and mCherry-labeled protein species are indicated in rows: (A, B, C) EGFP and mCherry-RXR, (D, E, F) EGFP and mCherry, (G, H, I) EGFP-HRas and mCherry, and (J, K, L) A3G-EGFP and mCherry.

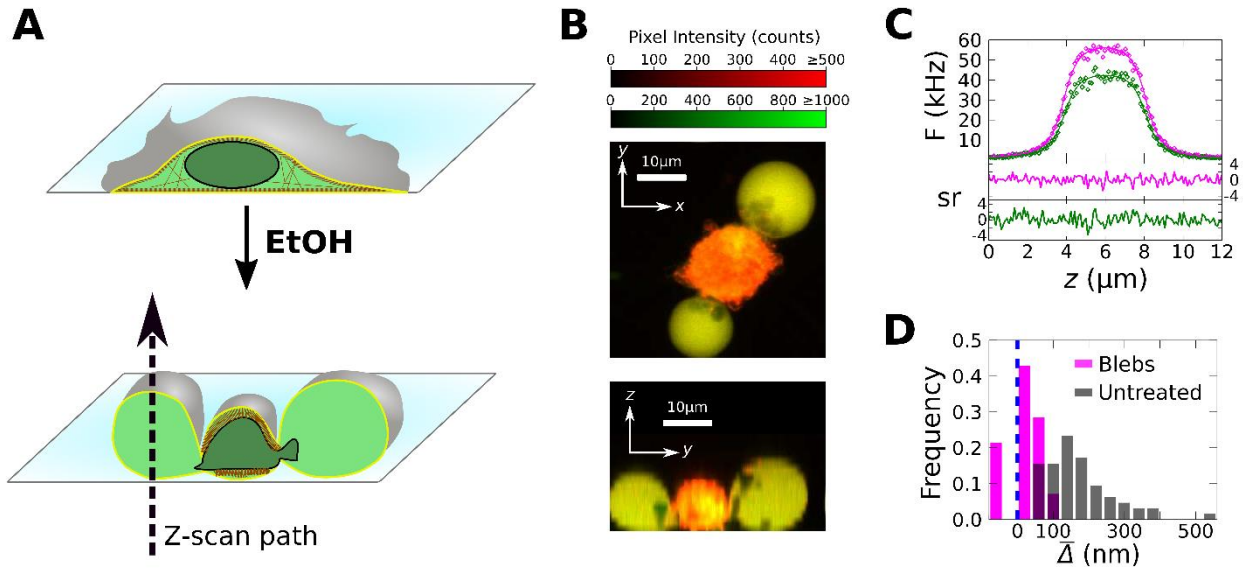

Fig. 2: Z-scans in blebs produced from HeLa cells co-expressing A3G-EGFP and mCherry. A) A graphic depicting the production of large PM blebs from adherent cells via ethanol treatment is shown. In this example, the cytoskeleton is denoted by brown colors. B) A DC 2-photon laser scanning z-stack image of a HeLa cell with two large PM blebs is shown. The x-y image was created by the summation of the z-stack over the z-dimension. The y-z image was produced by the sum of the x-dimension over two volume-sections passing roughly through the center of each bleb. While significant red autofluorescence is produced by the ethanol treatment near the cell center, it is typically absent in the blebs. Z-scan locations were selected to pass near the center of each bleb, while avoiding regions possessing autofluorescence or identifiable structures. C) Fit of a representative z-scan passing through a HeLa cell bleb (χ_ν^2= 1.2). D) Histogram of $\overline{\Delta}$ values in the cytoplasm of HeLa cells not treated with ethanol (magenta bars) and in blebs produced by ethanol treatment (gray bars).

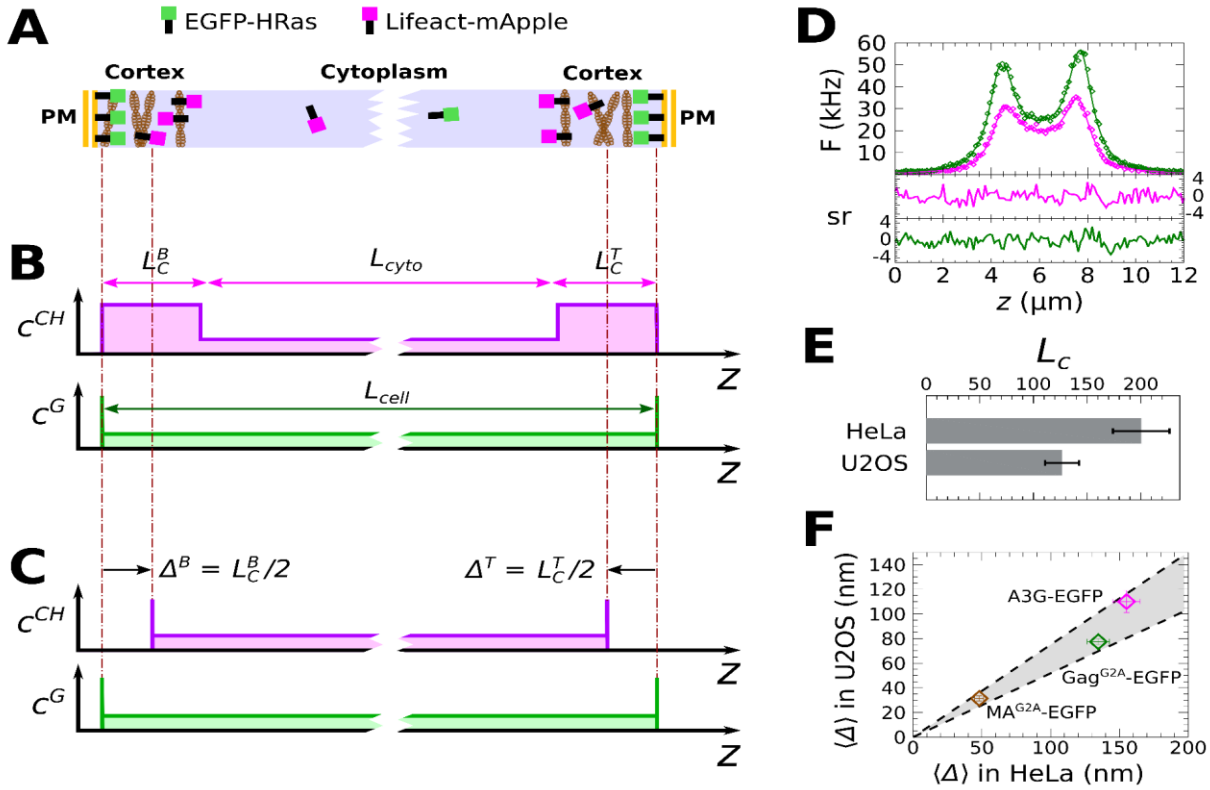

Fig. 3: DC z-scan measurement of cortex thickness. A) Lifeact-mApple demarcates the actin cortex, and EGFP-HRas demarcates the PM location. These fluorescent proteins lead to the SSS^{CH}-δSδ^{G} concentration profile depicted in (B). C) DC z-scans were fit to a δSδ^{CH}-δSδ^{G} model. The location of the mApple δ layers corresponds to the centroid of the cortical slabs, so that the effective depletion length is half the thickness of the cortex slab. D) A fit of a DC z-scan through a HeLa cell co-expressing EGFP-HRas and Lifeact-mApple. E) Average cortex thickness values estimated by DC z-scan in HeLa and U2OS cells. F) <*Δ*> is plotted in U2OS cells versus the same vales in HeLa cells for MA^{G2A}-EGFP (brown), Gag^{G2A}-EGFP (green) and A3G-EGFP (magenta). The ratio of cortex thicknesses in the cell lines corresponds to the slope of the data as is indicated by the shaded area and dashed lines, which correspond to the slope-uncertainty derived from the data in panel (E).

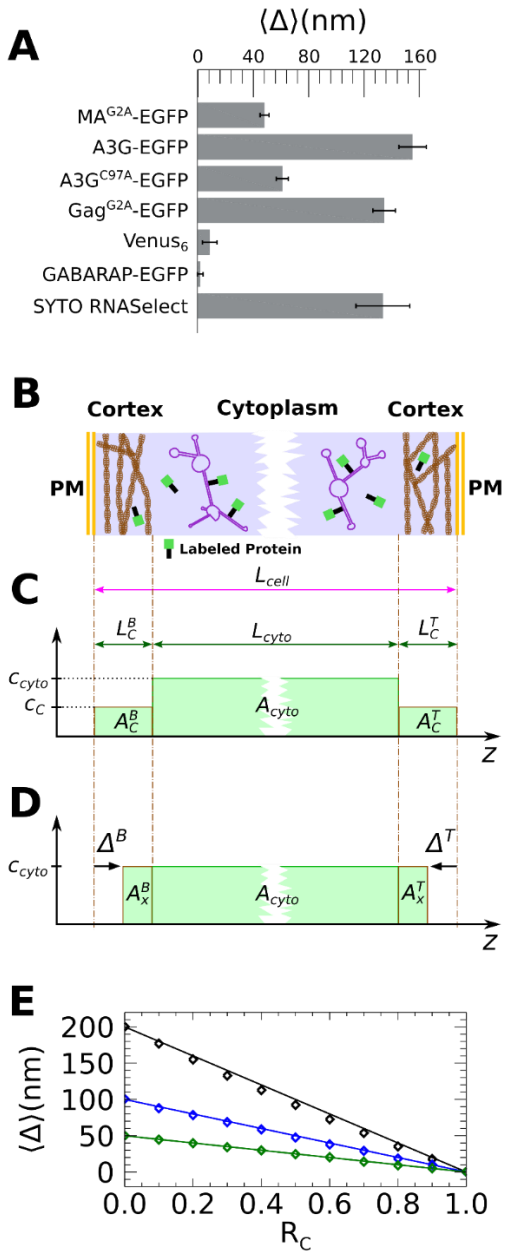

Fig. 4 Effective depletion length. A) <*Δ*> in HeLa cells for the indicated proteins and an RNA dye. B) Model of cortical partitioning leading to a SSS^G distribution of fluorescence. C) Axial concentration profile corresponding to the model. The concentration drops from c_{cyto} in the cytoplasm to c_C in the cortex. D) Approximation of the SSS^G by a single S^G concentration profile. Fitting of the experimental z-scan data to this profile was used to identify apparent depletion lengths Δ^B and Δ^T. The mCherry concentration profile has been omitted in panels C and D. E) <*Δ*> vs partition coefficient R_C extracted from simulated DC z-scans for three different cortex lengths ($L_C^B = L_C^T$ of 200, 100, and 50 nm). The solid lines represent a theoretical model based on Eq. 1.

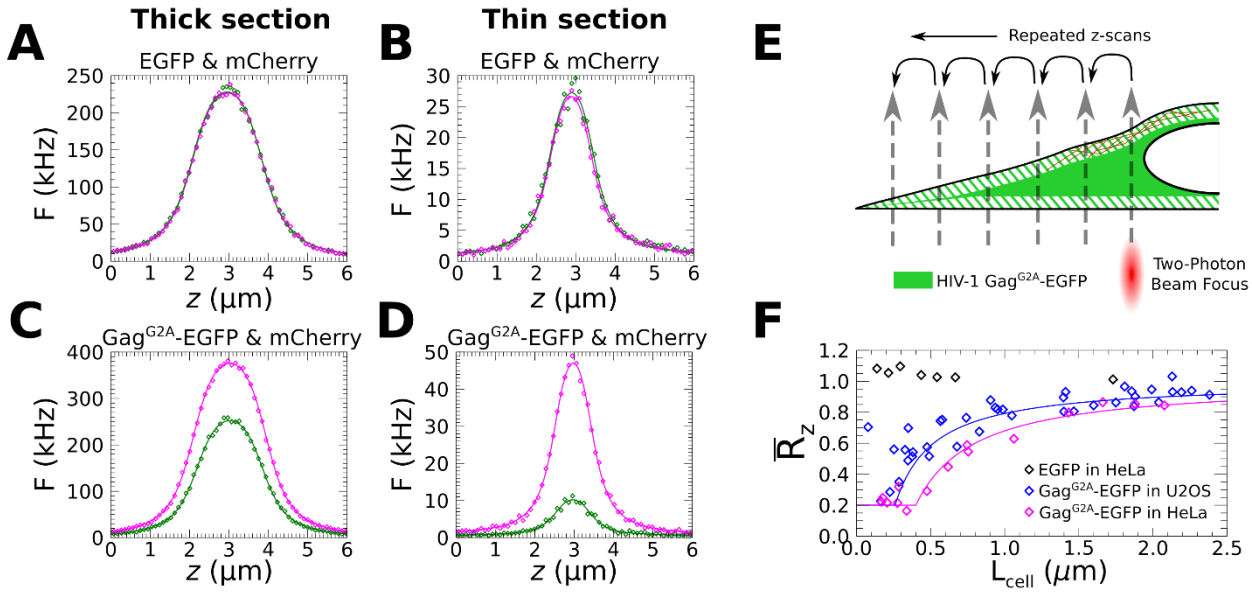

Fig. 5: Axially averaged partition coefficient $\bar{R}_z$ vs cell thickness. A-D) Representative DC z-scan traces in a thin and thick section of a HeLa cell co-expressing EGFP and mCherry (A, B) and representative DC z-scan traces in thin and thick sections of a HeLa cell co-expressing Gag^{G2A}-EGFP and mCherry. E) Schematic illustration of DC z-scans taken at multiple cytoplasmic locations varying from thick to thin sections to determine $\bar{R}_z$ as a function of thickness L_{cell}. F) $\bar{R}_z$ vs L_{cell}. Black diamonds correspond to control measurements in HeLa cells co-expressing EGFP and mCherry. Magenta and blue diamonds correspond to data from HeLa and U2OS cells co-expressing HIV-1 Gag^{G2A}-EGFP and mCherry. Magenta and blue lines correspond to Eq. 5 with $L_C = 200\ \text{nm}$ and $L_C = 130\ \text{nm}$, respectively, and $R_C = 0.2$.

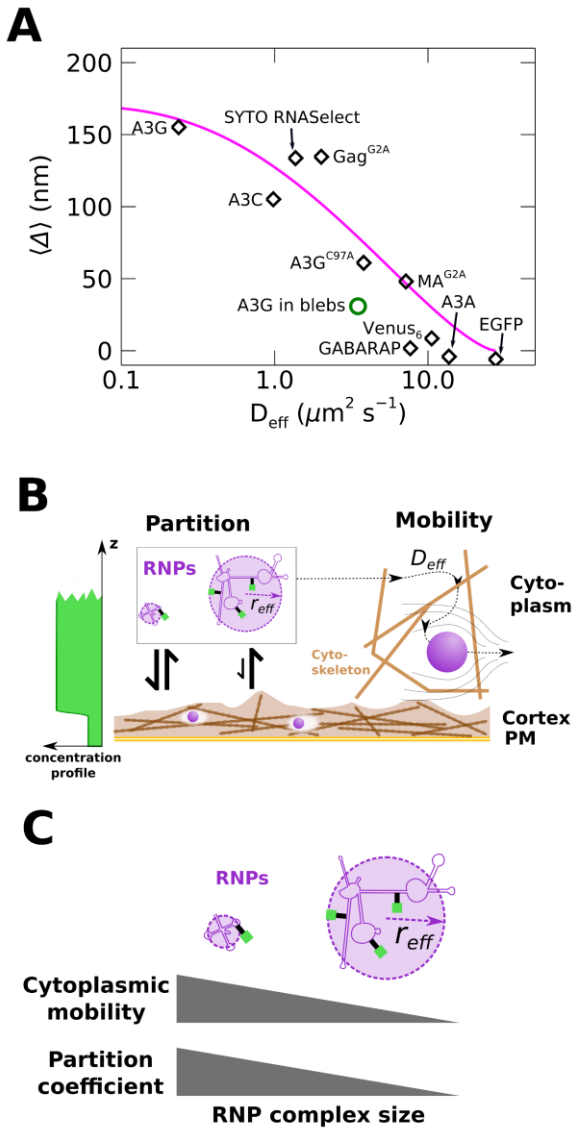

Fig. 6: Protein mobility and effective depletion length. A) Depletion length <Δ> versus effective diffusion coefficient D_{eff} in HeLa cells (diamonds). Eq. 8 (magenta curve) is plotted with parameter values as described in the text. A3G-EGFP measured in HeLa cell blebs (green open circle) displayed increased mobility along with decreased effective depletion length. B) Conceptual model of the effects quantified in panel A. The partitioning effect (center left) arises due to hindered entry of large RNP complexes into the cortical mesh, while hindered mobility of large RNP complexes due to macromolecular crowding occurs in the cytoplasm (right). Binding of labeled proteins to partitioned RNP complexes yields the concentration gradient (far left) observed by DC z-scan measurements. C) The cytoplasmic mobility and partition coefficient are connected by the average RNP complex radius, as indicated in the graphical depiction and suggested by Eqs. 7 and 8.